The Astrophysical Journal, 769:118 (12pp), 2013 June 1 doi:10.1088/0004-637X/769/2/118

THE *H*-BAND EMITTING REGION OF THE LUMINOUS BLUE VARIABLE P CYGNI: SPECTROPHOTOMETRY AND INTERFEROMETRY OF THE WIND

N. D. Richardson[1,9,10], G. H. Schaefer[2], D. R. Gies[1,10], O. Chesneau[3], J. D. Monnier[4], F. Baron[1,4], X. Che[4], J. R. Parks[1], R. A. Matson[1,10], Y. Touhami[1], D. P. Clemens[5], E. J. Aldoretta[1,10], N. D. Morrison[6], T. A. ten Brummelaar[2], H. A. McAlister[1], S. Kraus[7], S. T. Ridgway[8], J. Sturmann[2], L. Sturmann[2], B. Taylor[5], N. H. Turner[2], C. D. Farrington[2], and P. J. Goldfinger[2]

[1] Center for High Angular Resolution Astronomy, Department of Physics and Astronomy, Georgia State University, P.O. Box 4106, Atlanta, GA 30302-4106, USA; richardson@astro.umontreal.ca
[2] The CHARA Array, Georgia State University, P.O. Box 3965, Atlanta, GA 30302-3965, USA
[3] Nice Sophia-Antipolis University, CNRS UMR 6525, Observatoire de la Côte d'Azur, BP 4229, F-06304 Nice Cedex 4, France
[4] Department of Astronomy, University of Michigan, 941 Dennison Bldg., Ann Arbor, MI 48109-1090, USA
[5] Institute for Astrophysical Research, Boston University, 725 Commonwealth Ave., Boston, MA 02215, USA
[6] Ritter Astrophysical Research Center, Department of Physics and Astronomy, University of Toledo, 2801 W. Bancroft, Toledo, OH 43606, USA
[7] University of Exeter, Astrophysics Group, Stocker Road, Exeter, EX4 4QL, UK
[8] National Optical Astronomical Observatory, 950 North Cherry Ave., Tucson, AZ 85719, USA
Received 2013 February 7; accepted 2013 April 3; published 2013 May 14

ABSTRACT

We present the first high angular resolution observations in the near-infrared *H* band (1.6 μm) of the luminous blue variable star P Cygni. We obtained six-telescope interferometric observations with the CHARA Array and the MIRC beam combiner. These show that the spatial flux distribution is larger than expected for the stellar photosphere. A two-component model for the star (uniform disk) plus a halo (two-dimensional Gaussian) yields an excellent fit of the observations, and we suggest that the halo corresponds to flux emitted from the base of the stellar wind. This wind component contributes about 45% of the *H*-band flux and has an angular FWHM = 0.96 mas, compared to the predicted stellar diameter of 0.41 mas. We show several images reconstructed from the interferometric visibilities and closure phases, and they indicate a generally spherical geometry for the wind. We also obtained near-infrared spectrophotometry of P Cygni from which we derive the flux excess compared to a purely photospheric spectral energy distribution. The *H*-band flux excess matches that from the wind flux fraction derived from the two-component fits to the interferometry. We find evidence of significant near-infrared flux variability over the period from 2006 to 2010 that appears similar to the variations in the Hα emission flux from the wind.

Key words: circumstellar matter – stars: early-type – stars: individual (P Cyg, HD 193237) – stars: mass-loss – stars: variables: S Doradus – stars: winds, outflows

Online-only material: color figures

1. INTRODUCTION

Luminous blue variables (LBVs or S Doradus variables) are evolved, massive stars that are characterized by large mass-loss rates and variability on multiple timescales. Humphreys & Davidson (1994) estimate that the typical mass-loss rate of a non-erupting LBV is of the order of $\dot{M} \approx 10^{-5}$–$10^{-3}\ M_\odot\ \mathrm{yr}^{-1}$. The lifetime in the LBV phase is uncertain, but is on the order of 25,000 yr. One of the defining criteria of the LBVs is the detection of a large-scale eruption, when the star brightens by several magnitudes. The quiescent times between these eruptions may last centuries. In addition to such rare, giant eruptions, these stars also display lesser photometric and spectroscopic variations on other timescales, ranging from days to decades or centuries (van Genderen 2001). The two "prototypical" Galactic LBVs are η Car and P Cygni, and they probably represent different extremes of both mass and mass-loss rate within the scheme of LBV evolution (Israelian & de Groot 1999).

The basic properties of P Cygni (HD 193237, HR 7763, and Nova Cyg 1600) were estimated by Najarro et al. (1997) and Najarro (2001) by comparing ultraviolet, optical, and infrared spectroscopic observations with results from the non-LTE atmospheric modeling code CMFGEN (Hillier & Miller 1998). Najarro et al. found that P Cyg has a mass-loss rate of $3.2 \times 10^{-5}\ M_\odot\ \mathrm{yr}^{-1}$, a terminal wind speed of 185 km s^{-1}, a distance of 1.7 ± 0.1 kpc, and an assumed continuum forming radius of $75\ R_\odot$. The star has a luminosity of (5.6–7.0) $\times\ 10^5\ L_\odot$, effective temperature of (18.1–19.2) kK, and a gravity $\log g_{\mathrm{eff}} = 1.20$. Their models of the hydrogen and helium spectral lines in the UV to near-infrared (NIR) wavelength range yield a fractional composition of $n_{\mathrm{He}}/n_{\mathrm{H}} = 0.3$, indicating that nuclear processed gas is present in the photosphere. The model presented in Najarro (2001) also gives estimates of the abundances of C, N, O, Mg, Al, Si, Fe, Co, and Ni. Most of these elements have near solar metallicity, but C and O are depleted ($N_{\mathrm{C}}/N_{\mathrm{C}_\odot} = 0.3$ and $N_{\mathrm{O}}/N_{\mathrm{O}_\odot} = 0.18$) and N is enriched relative to solar ($N_{\mathrm{N}}/N_{\mathrm{N}_\odot} = 6.5$).

Richardson et al. (2011) examined the optical variability (*V*-band photometry and Hα spectroscopy) of P Cyg following the earlier study of Markova et al. (2001). Both studies found that the Hα emission line increases and decreases in concert with the *V*-band flux. The variability in the *V* band is due to the

[9] Current address: Département de Physique and Centre de Recherche en Astrophysique du Québec (CRAQ), Université de Montréal, C.P. 6128, Succ. Centre-Ville, Montréal, QC H3C 3J7, Canada.
[10] Visiting Astronomer, Lowell Observatory.

portion of the optical flux that originates in the stellar wind, but some variability may also be due to the pulsation properties of the star (e.g., Percy et al. 2001). Furthermore, Richardson et al. discovered that there were "discrete absorption components" in the P Cygni absorption trough of the Hα line profile that moved blueward with time, indicative of accelerating matter in our line of sight. These were long-lived features (2–3 yr), with a possible recurrence time of ~4.7 yr. This absorption strength increases when V is brighter and Hα is stronger. The absorption variations (formed in the gas column projected against the star) matched those of the continuum and line emission (formed in a large volume surrounding the star), and that was interpreted as evidence that the structure of the wind in our direction is comparable to that in other directions, i.e., that the wind is spherical in geometry.

High angular resolution techniques can aid our understanding of the stellar winds through measurements of the geometry of the outflows. Stellar winds around hot, massive stars are a source of infrared and radio flux from free–free and bound-free processes. Because the optical depth of the wind increases with wavelength, the observed diameter of the star will appear larger at longer wavelengths (e.g., Lamers & Cassinelli 1999). The advent of long-baseline optical and NIR interferometry provides a method of directly measuring the extent of emitting regions and determining the amount of flux excess at longer wavelengths. Such studies can be compared to models of stellar atmospheres and winds, such as those of Hillier & Miller (1998; CMFGEN). For example, Weigelt et al. (2007) found evidence of an asymmetric wind from the enigmatic LBV η Car using VLTI/AMBER interferometry.

Three key studies have used high angular resolution techniques to examine the Hα emission of P Cygni. Vakili et al. (1997) used the Grand Interférométre à 2 Télescopes (GI2T) to resolve an Hα emitting region of angular diameter 5.5 ± 0.5 mas, which corresponds to 14 R_* for the stellar diameter and distance derived by Najarro et al. (1997). A similar result was recently obtained by Balan et al. (2010) based upon observations made with the Navy Precision Optical Interferometer. They compared the angular extent of the Hα emission region to that of the nearby continuum and then derived an Hα emitting region that was 3–7 mas in diameter. The Hα emission from the outer region of the wind was explored using adaptive optics techniques by Chesneau et al. (2000), who made a reconstructed image that shows a faint and clumpy halo with a radius of ~200 mas. The wind structure on the largest scales was examined through radio observations by Skinner et al. (1997, 1998). Their studies resolved circumstellar structures that extend to an angular size of ~1′. The structures show a clumpy and/or filamentary appearance. Skinner et al. developed a spherically symmetric wind model for the resolved radio nebula, and while they were able to obtain a good fit to the spectral energy distribution (SED), their model did not explain the structure present in the observations.

Here, we investigate the wind of P Cygni through a comparison of Hα spectroscopy, NIR H- and K-band spectrophotometry, and interferometric H-band measurements from the CHARA Array using the MIRC beam combiner. We outline our spectroscopic measurements in Section 2, and in Section 3 we discuss our interferometric measurements and an image reconstruction based upon these data. We discuss these results and offer conclusions from our study in Section 4.

2. SPECTROSCOPY AND PHOTOMETRY

We collected high-resolution Hα spectroscopy and NIR spectrophotometry within 2–3 weeks of our interferometric observations. The Hα spectra were obtained from two observatories. The first set of two spectra was obtained at the University of Toledo's Ritter Observatory with the 1 m telescope and échelle spectrograph (Morrison et al. 1997). The detector was a Spectral Instruments 600 Series camera, with a front-illuminated Imager Labs IL-C2004 4100 × 4096 pixel sensor (15 × 15 μm pixels). Wavelength calibration was accomplished with a Th–Ar discharge lamp. These high resolving power ($R = 26{,}000$) spectra were reduced using standard techniques with IRAF[11] with bias frames and flat fields obtained on the same night. We reduced three orders of échelle data, which span 6285–6443 Å, 6470–6633 Å, and 6666–6834 Å. The resulting signal-to-noise ratio is roughly 100 in the continuum near Hα.

A second set of five Hα spectra was obtained at Georgia State University's Hard Labor Creek Observatory (HLCO). The data were collected with a 0.5 m RC Optical Systems telescope[12] and an LHIRES III spectrograph.[13] These spectra were recorded on a thermoelectrically cooled SBIG-ST8XME CCD. The dispersion was accomplished with gratings of either 2400 grooves mm^{-1} ($R \sim 18{,}000$) or 600 grooves mm^{-1} ($R \sim 4500$). These data were reduced with standard techniques in IRAF utilizing bias, dark, and flat fields. Wavelength calibration was accomplished with a built-in Ne discharge lamp in the spectrograph.

A log of the Hα measurements is listed in Table 1, along with contemporaneous photoelectric V-band measurements from the American Association for Variable Star Observers (AAVSO). The equivalent widths of the Hα profiles were measured by integration between 6510 and 6617 Å for all spectra, which is the same range used by Markova et al. (2001). Changes in the continuum flux can cause apparent equivalent width variations (based upon the changing ratio of emission to continuum flux), so we corrected for the variable continuum in the same manner as done by Markova et al. (2001) and Richardson et al. (2011) using the V-band estimates in Table 1, i.e.,

$$W_\lambda(\mathrm{corr}) = W_\lambda(\mathrm{net}) 10^{-0.4(V(t)-4.8)}.$$

We obtained a single epoch of NIR spectrophotometry (Table 2) in the K and L bands in 2006 with the NASA Infrared Telescope Facility and SpeX cross-dispersed spectrograph (Rayner et al. 2003). This observation (reported earlier by Touhami et al. 2010) was collected with a 3″ wide slit. We also obtained five epochs of NIR spectrophotometry in the H and K bands using the Mimir instrument on Lowell Observatory's Perkins telescope (Clemens et al. 2007) between 2008 and 2011. These observations were obtained with a 10″ wide slit. These spectra were made by combining at least 10 individual spectra obtained by dithering along the slit.

Reductions of the SpeX spectrum were carried out with the `SpeXtool` package (Vacca et al. 2003; Cushing et al. 2004). Reductions of the Mimir data were accomplished using custom software[14] that used bias, dark, and flat field frames.

[11] IRAF is distributed by the National Optical Astronomy Observatory, which is operated by the Association of Universities for Research in Astronomy, Inc., under cooperative agreement with the National Science Foundation.
[12] http://www.rcopticalsystems.com/telescopes/20truss.html
[13] http://www.shelyak.com/rubrique.php?id_rubrique=6&lang=2
[14] Available for download at http://people.bu.edu/clemens/mimir/software.html.

Table 1
Hα Spectroscopy

UT (YYYY-MM-DD) (1)	Source (2)	Date (HJD −2,400,000) (d) (3)	R (4)	W_λ (net) (Å) (5)	V (mag) (6)	W_λ (corr) (Å) (7)
2008-10-22	Ritter	54762	26,000	−87.4	4.72	−94.1
2010-08-29	Ritter	55438	26,000	−85.8	4.81	−85.0
2011-05-10	HLCO	55692	4,500	−89.6	4.67	−101.0
2011-05-24	HLCO	55706	18,000	−86.7	4.67	−97.7
2011-06-14	HLCO	55727	4,500	−86.2	4.62	−101.7
2011-06-21	HLCO	55734	4,500	−84.1	4.58	−103.0
2011-08-16	HLCO	55790	4,500	−89.6	4.66	−101.9

Table 2
NIR Spectrophotometry

UT Date (YYYY-MM-DD) (1)	Observatory/ Instrument (2)	Date (HJD −2,400,000) (d) (3)	$\log(F_H)$ (1.629 μm) (erg s^{-1} cm^{-2} Å^{-1}) (4)	$\triangle H$ (1.629 μm) (mag) (5)	$\log(F_K)$ (2.179 μm) (erg s^{-1} cm^{-2} Å^{-1}) (6)	$\triangle K$ (2.179 μm) (mag) (7)
2006-09-16	IRTF/SpeX	53994	...	...	−11.62	0.72
2008-10-20	Lowell/Mimir	54759	−11.21	0.64	−11.57	0.86
2009-07-13	Lowell/Mimir	55025	−11.27	0.48	−11.62	0.73
2009-11-06	Lowell/Mimir	55141	−11.31	0.38	−11.66	0.63
2010-07-03	Lowell/Mimir	55380	−11.25	0.55	−11.59	0.81
2010-11-27	Lowell/Mimir	55527	−11.25	0.55	−11.60	0.80
...	MODEL	...	−11.46	0.00	−11.91	0.00

We corrected for the Mimir detector's non-linearity through a series of flat fields obtained on the same observing run to establish the response of each pixel to increasing exposure time (Clemens et al. 2007). The Mimir and SpeX spectra were transformed to an absolute flux scale (and corrected for telluric absorption) using the *xtellcor* package (Vacca et al. 2003). This method uses flux calibrator stars of spectral type A0 V (in this case HD 192538) that are transformed to flux through reference to a model Vega spectrum calculated by R. Kurucz. The transformation takes into account rotational broadening, interstellar extinction, and the B and V magnitudes of the calibrator (in this case, $B = 6.48$, $V = 6.45$). A log of the NIR spectrophotometry is given in Table 2. Note that the spectrophotometry obtained in 2006 and 2008 was previously published by Touhami et al. (2010). All optical and NIR spectra are available upon request.

The H- and K-band spectra are plotted in Figure 1, and their relative flux placements confirm the temporal variability found by Touhami et al. (2010). Figure 1 also shows the predicted photospheric SED from a Kurucz model that was normalized to the blue part of the spectrum where the wind contributes little flux (Touhami et al. 2010). During the course of our observations, the flux excess relative to the photospheric SED varied between 0.38 and 0.64 mag in the H band and between 0.63 and 0.86 mag in the K band.

In addition to the optical Hα spectroscopy and the NIR spectrophotometry, we collected V-band data from the AAVSO and the recent analysis of Pollmann & Bauer (2012). Figure 2 shows a comparison of the variations over the past six years in the V-band magnitude, Hα emission equivalent width, and IR flux excesses. The AAVSO photoelectric photometry measurements agree well with the V-band measurements of Pollmann & Bauer (2012), and they show that a local fading occurred around 2010.0 that was followed by a gradual increase in brightness. Some of the V-band measurements from Pollmann & Bauer (2012) were also reported to the AAVSO, so we removed the duplicate points from the AAVSO data set shown in Figure 2. The Hα equivalent widths from Balan et al. (2010), Richardson et al. (2011), and Pollmann & Bauer (2012) are shown together with our new measurements in the middle panel (all corrected for the changing continuum). These show many of the same trends seen in the V-band data, and we show a long-term running average of the measurements in the top two panels to illustrate this. This was calculated using a Gaussian weighting scheme parameterized by an FWHM of 300 days. The lower panel shows the H- and K-band flux excesses in the same format, and these quantities show evidence that they are correlated with the V-band magnitudes and Hα emission strengths (in particular showing the same fading near 2010.0). These trends suggest that all four of these quantities vary in concert according to changes in the mass-loss rate, as suggested in the analysis of Richardson et al. (2011). With more NIR data, future analyses may show a direct correlation between the NIR and visual magnitudes.

3. INTERFEROMETRY

3.1. Observations

We obtained interferometric observations of P Cyg on three nights, two in 2010, and one in 2011, using the MIRC beam combiner (Monnier et al. 2004, 2006) at the CHARA Array (ten Brummelaar et al. 2005). We observed with MIRC using the low-resolution prism ($R \sim 42$), which disperses the light across eight spectral channels in the H band (1.50–1.75 μm; $\Delta\lambda \sim 0.034\,\mu$m for each spectral channel). Table 3 presents a log of the observing dates, telescope configurations, range of baseline lengths, and observed calibrators. On 2010 August 21 and 23, we combined the light from three and four telescopes, respectively. On 2011 September 3, we combined the light from all six telescopes simultaneously. All observations made use of the photometric channels installed on MIRC, which

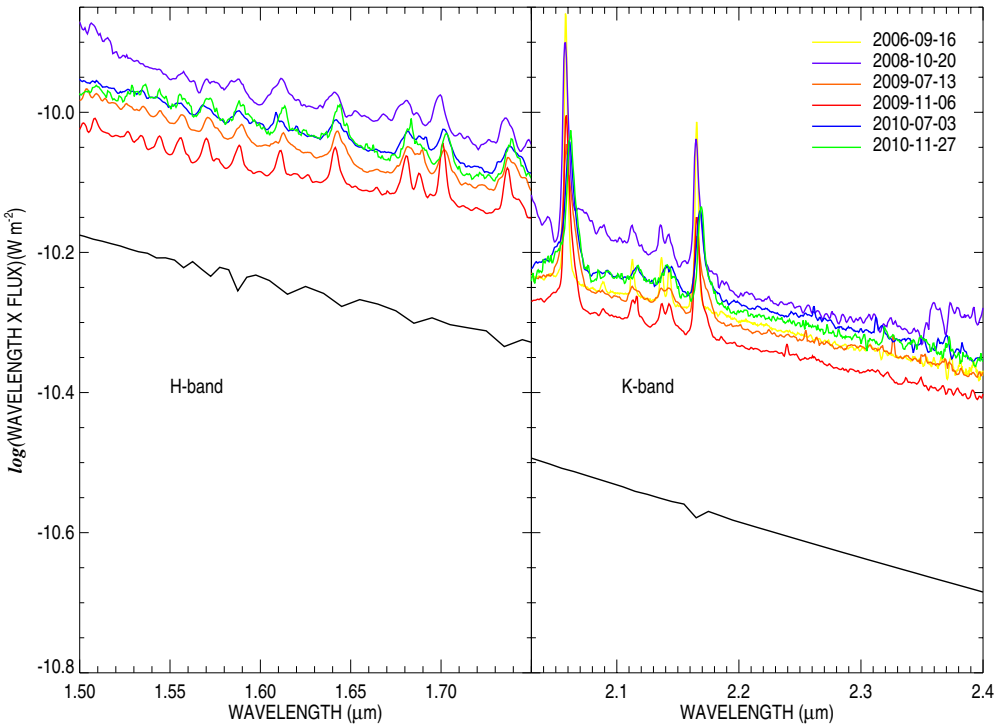

Figure 1. *H*- (left) and *K*-band (right) spectrophotometry. Dates are given in the legend and match the observations listed in Table 2. The (black) spectrum of low flux is the Kurucz model used to determine the IR excess.

(A color version of this figure is available in the online journal.)

Table 3
CHARA/MIRC Observations

UT Date (YYYY-MM-DD)	Telescope Designations	Min. Baseline (m)	Max. Baseline (m)	Calibrator Names
2010-08-20	S1-W1-W2	108	279	σ Cyg, ζ Cas
2010-08-23	S2-E2-W1-W2	108	251	σ Cyg, 7 And, ζ Cas
2011-09-03	S1-S2-E1-E2-W1-W2	34	331	σ Cyg, 7 And, θ Cas

Table 4
Adopted Angular Diameters for the Calibrators

Name	HD	θ_{LD} (mas)	Reference
σ Cyg	202850	0.574 ± 0.017	1
7 And	219080	0.659 ± 0.017	2, 3, 4, 5
ζ Cas	3360	0.307 ± 0.021	6
θ Cas	6961	0.608 ± 0.019	7

References. (1) Schaefer et al. 2010; (2) Che et al. 2011; (3) Barnes et al. 1978; (4) Bonneau et al. 2006; (5) Kervella & Fouqué 2008; (6) Zorec et al. 2009; (7) Gies et al. 2007.

measure directly the contribution of light from each telescope and improve the visibility and closure phase calibration (Che et al. 2010).

To measure the instrument response, we observed calibrator stars with angular diameters smaller than 0.7 mas. On each night, we observed σ Cyg as the primary calibrator; we also used calibrators observed a couple of hours following the P Cyg observations to monitor the stability of the visibility calibration. The adopted limb-darkened diameters (θ_{LD}) of the calibrators are listed in Table 4. The data were reduced using the standard MIRC reduction pipeline (Monnier et al. 2007). The visibilities and closure phases were averaged over the 2–3 minute observing blocks. Based on an overall assessment of the data quality obtained with MIRC using the photometric channels, we applied minimum baseline uncertainties of 5% to the squared visibilities and 0.°3 to the closure phases. The calibrated OIFITS data files (Pauls et al. 2005) are available on request.

Figure 3 shows the (u, v) coverage on the sky sampled by the CHARA Array during the three nights of the P Cyg observations obtained with MIRC. Figure 4 shows a plot of the squared visibilities measured with MIRC during all three nights. The visibilities drop steadily with increasing baseline, and so with spatial frequency, indicating that the object is mostly symmetric and resolved on the longest baselines. Figure 5 shows the closure phases measured on each closed triangle. There are small non-zero closure phases ($\sim 2^\circ$) on some triangles, possibly indicating the presence of a small asymmetry in the light distribution.

3.2. Geometric Models

Our results in Figure 2 show that the star's Hα emission was stronger during the 2011 CHARA observations than during the 2010 CHARA observation. However, the visibilities measured by CHARA/MIRC for both sets in the *H* band are comparable. Therefore, in addition to fitting the data from each epoch separately, we also combined the two CHARA data sets to constrain better the models. As Figure 6 shows, we fit three

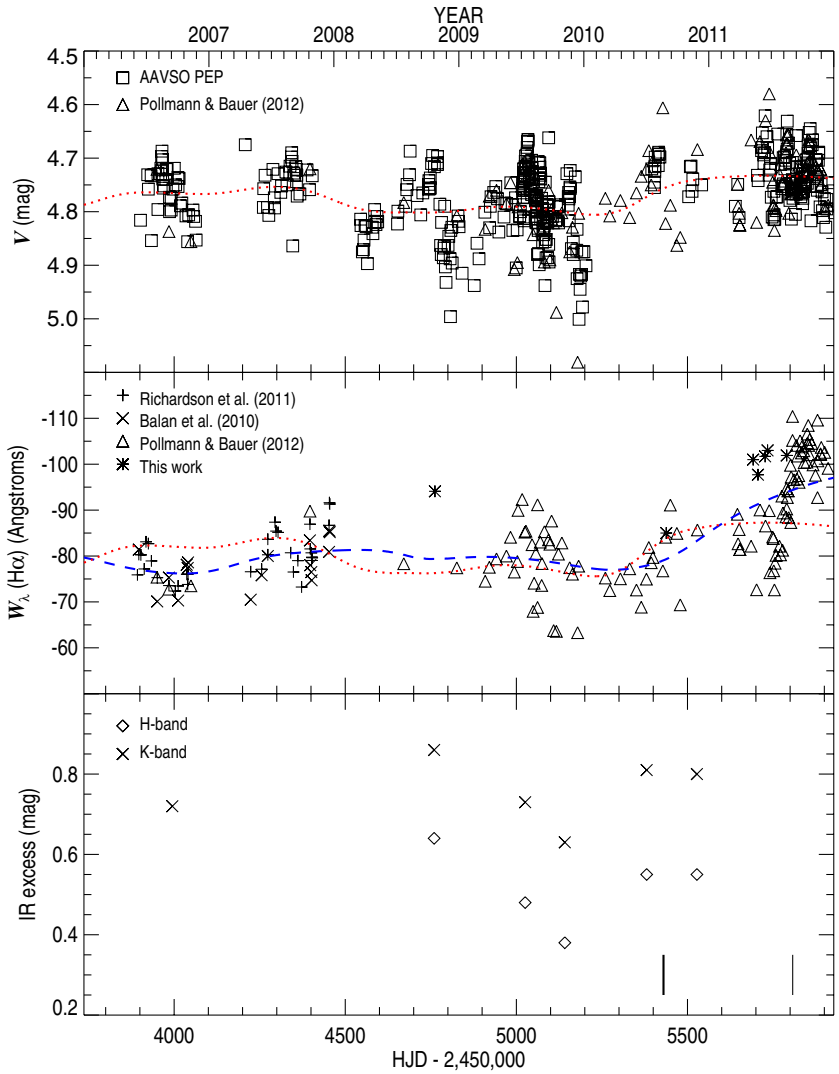

Figure 2. *V*-band photometry from the AAVSO and Pollmann & Bauer (2012) is shown in the top panel (note that many of the measurements of Pollmann & Bauer were also reported to the AAVSO, making the data sets have some overlap, so only those measurements from Pollmann & Bauer are shown in such cases), Hα equivalent width (corrected for a changing continuum) in the middle panel, and the *HK*-band IR excesses in the bottom panel. We overplotted a running average of the *V*-band flux (red dotted line) in both the top and middle panels, as well as a similar curve (blue dashed line) for the Hα measurements in the second panel to show the similarity of the variability of these measurements. The epochs of CHARA/MIRC observations are marked with vertical lines in the bottom panel.

(A color version of this figure is available in the online journal.)

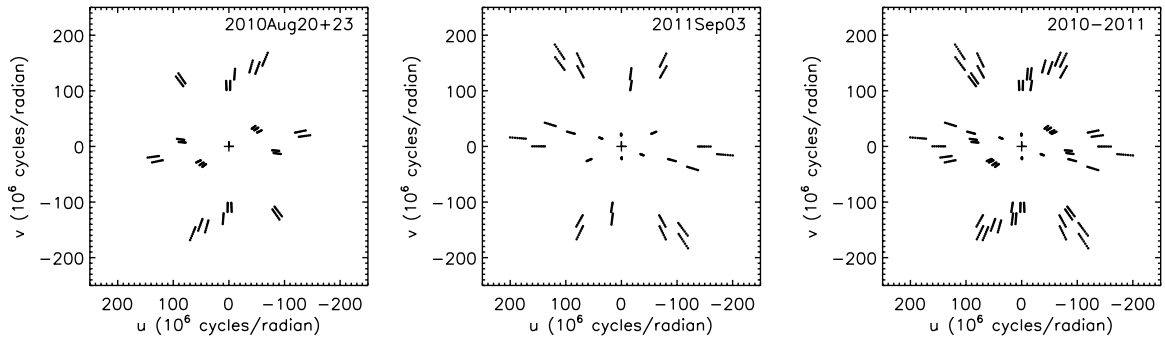

Figure 3. (u, v) coverage during the MIRC observations of P Cyg for the 2010 and 2011 data, as well as for the combined data set.

types of geometrical models to the interferometric visibilities: a single uniform disk, a single circularly symmetric Gaussian, and a two-component model where the star is represented as a uniform disk and the extended wind emission is represented by a circular Gaussian centered on the star. In the two-component model, we fixed the stellar disk diameter at $\theta_{\rm UD} = 0.411$ mas (75 $R_\odot$ at 1.7 kpc), as found by Najarro et al. (1997) and Najarro (2001), and solved for the FWHM size of the Gaussian wind ($\theta_{\rm FWHM}$) and the flux ratio between the wind and the star ($f_{\rm wind}/f_{\rm star}$).

Table 5 lists the results for the 2010 and 2011 epochs separately as well as for the combined data set. In Figure 4,

Table 5
Model Fit Results

Parameter	UT 2010 Aug 20+23	UT 2011 Sep 3	Combined Fit
	Uniform disk model		
θ_{UD} (mas)	0.902 ± 0.007	0.838 ± 0.004	0.858 ± 0.005
χ^2_ν	6.21	9.28	9.04
	Circularly symmetric Gaussian model		
θ_{FWHM} (mas)	0.558 ± 0.004	0.524 ± 0.003	0.536 ± 0.003
χ^2_ν	4.57	5.83	5.99
	Two-component model: uniform disk and circular Gaussian		
f_{wind}	0.396 ± 0.014	0.475 ± 0.020	0.450 ± 0.018
$f_{corr,wind}$[a]	0.379	0.443	0.423
θ_{FWHM} (mas)	1.121 ± 0.027	0.898 ± 0.022	0.964 ± 0.022
f_{star}	0.604 ± 0.014	0.525 ± 0.020	0.550 ± 0.018
$f_{corr,star}$[a]	0.621	0.557	0.577
θ_{UD} (mas)	0.41 (fixed)	0.41 (fixed)	0.41 (fixed)
χ^2_ν	0.69	1.13	1.13
Num. Vis.	120	120	240

Note. [a] These values correspond to the corrected flux where flux from a circular Gaussian wind behind the star would be blocked from our line of sight, so half of the flux in the Gaussian coincident with the star is subtracted from the wind and added to the star.

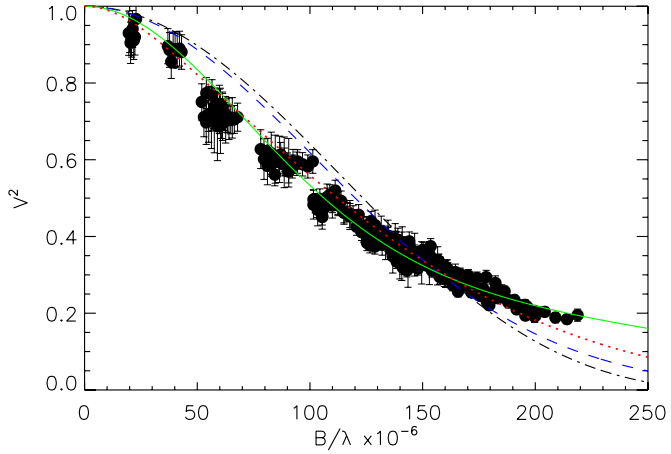

Figure 4. Calibrated visibilities measured for P Cyg using MIRC on UT 2010 August 20+23 and 2011 September 3. The black dashed-dotted line is the best-fit uniform disk model, the blue dashed line represents the best Gaussian model, the solid green line is our two-component model, and the dotted red line is the rescaled CMFGEN model (see discussion).

(A color version of this figure is available in the online journal.)

the comparison of the models to the visibilities demonstrates the superiority of the two-component model. In both epochs as well as the combined data set, the χ^2_ν is significantly improved in the two-component model compared with a single uniform disk or a single circular Gaussian. We attempted to fit an elliptical Gaussian to the data as well, but we found that the χ^2 of the fit was not improved significantly. Moreover, the difference between the FWHM of the major and minor axes was less than 5%, with a deviation of less than 1.2σ, suggesting that the wind is essentially circular in the H-band continuum.

Figure 6 shows images of the best-fit models for the uniform disk, circular Gaussian, and the two-component model for the combined data set. The best-fit two-component model for the combined 2010 and 2011 data sets gives a wind FWHM size of 0.96 ± 0.02 mas ($R = 2.3R_*$), contributing approximately 45% of the total flux. The parameter uncertainties quoted in Table 5 include the small spread in the results due to the uncertainties in the assumed photospheric angular diameter ($\triangle\theta_{UD}/\theta_{UD} \approx 3\%$). Our geometric model assumes that the circular Gaussian representing the wind is centered on the star. The star may in fact block flux from the wind behind the star. To account for this effect, we calculated the total flux in the wind that is coincident with the star (f_{cent}). We corrected the flux contributions by removing $0.5f_{cent}$ from the wind component and adding $0.5f_{cent}$ to the stellar flux (to roughly account for the foreground/background portions of the wind). After applying this correction, we find that the wind contribution drops to 42% of the total flux in the combined data set.

We attempted to fit for the uniform disk diameter of the star as a free parameter in the two-component model, but the results were not consistent between epochs, with values ranging from 0.39 to 0.62 mas. The resolution of the CHARA Array on the longest baseline in the H band is ~0.52 mas; therefore, the stellar diameter is only marginally resolved and would require a more precise calibration of the interferometric visibilities to measure reliably. The situation is further complicated by model degeneracies between the stellar diameter, size of the wind, and flux contribution of each component. For instance, assuming a larger stellar angular diameter results in a model that contains a fainter but more extended wind. Because we fixed the stellar diameter over a narrower range of parameter space than is allowed for by the interferometric data alone, we suspect that the uncertainties listed in Table 5 do not fully represent the model degeneracies. Therefore, differences in the parameters between the two epochs should not be treated as significant. Additionally, the sampling of the (u, v) coverage may affect the parameters of the fit. We note that the reduced χ^2_ν of the combined fit is close to 1, indicating that the model does a good job reproducing the data from each epoch.

3.3. Image Reconstructions

Figure 5 shows the closure phases measured with the MIRC beam combiner at the CHARA Array. The small, but non-zero, closure phases show that there may be some structure in the wind. The geometric models computed in Section 3.2 are point-symmetric and do not account for the non-zero closure

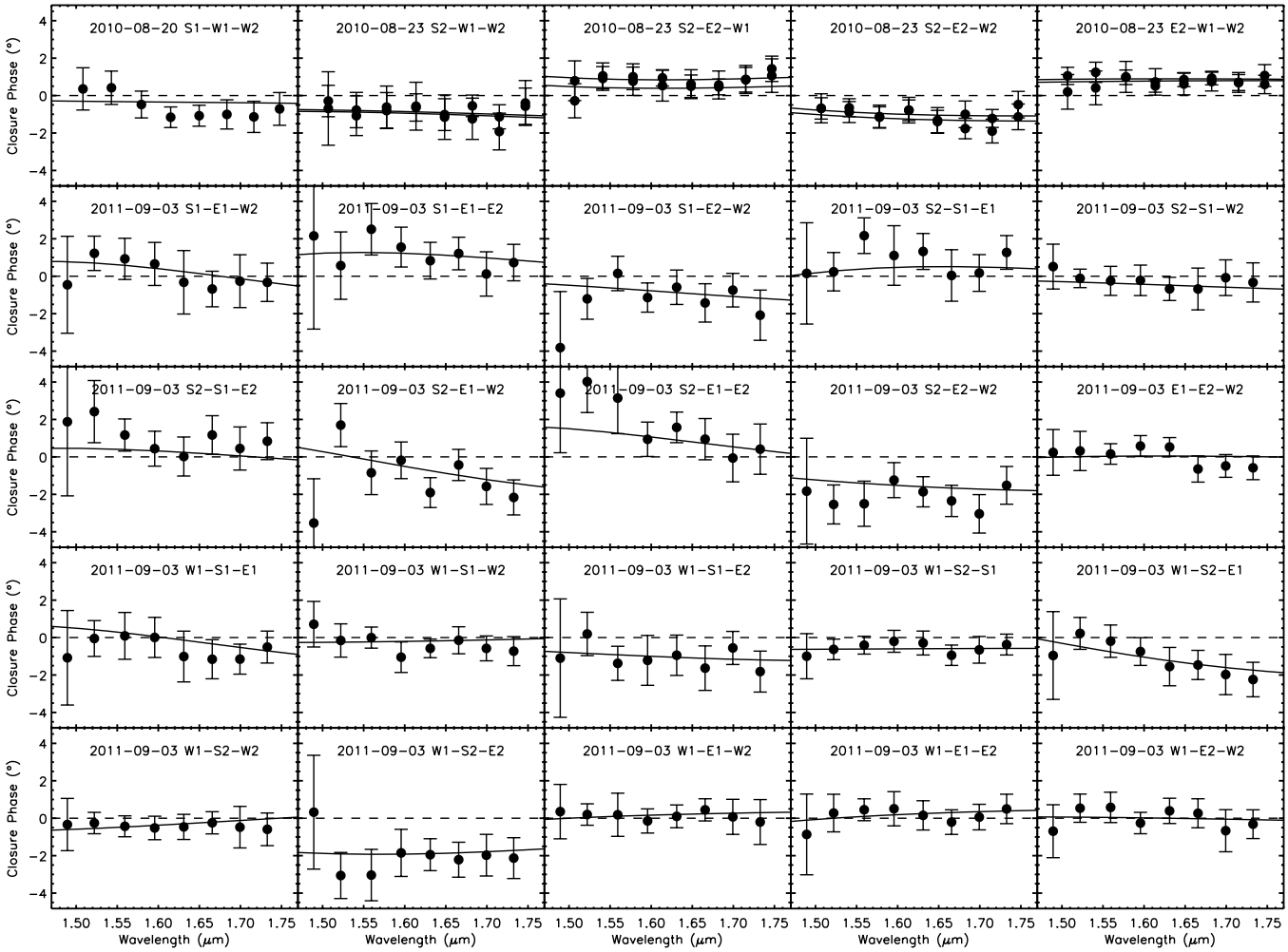

Figure 5. Closure phases measured for P Cyg using MIRC on UT 2010 August 20+23 and 2011 September 3. The solid lines show the closure phases associated with the reconstructed image in the lower-left panel of Figure 7. On 2010 August 23, we obtained two observations on P Cyg separated in time by about 30 minutes. There is a small amount of rotation in the (u, v) plane between these observations that samples the reconstructed image in a slightly different way. The two solid lines in the plots for this date show the reconstructed closure phases for each data point. On 2010 August 20 and 2011 September 3 we only obtained one observation of P Cyg.

phases. We attempted to map the asymmetry by reconstructing images of P Cygni using the MArkov Chain IMager (MACIM; Ireland et al. 2006) and BiSpectrum Maximum Entropy Method (BSMEM; Baron & Young 2008) software packages. MACIM randomly moves flux within a pixel grid to reconstruct the image; the movement is regulated by a simulated annealing temperature. BSMEM uses a gradient descent method to converge to the best image.

Examples of different image reconstructions of P Cygni based on the MIRC data from 2010 to 2011 are shown in Figure 7. We combined the epochs to maximize the (u, v) coverage, but also reconstructed images for each epoch separately to avoid potentially blurring the motion of structures within the wind. The top row of Figure 7 shows a comparison of images reconstructed using BSMEM and MACIM. For the BSMEM reconstruction, we started with the initial image and a prior set to a 2.0 mas Gaussian. Note that the initial image defines the starting position of the flux distribution, while the prior image defines the probability of where the flux is likely to move during the reconstruction. For the MACIM reconstruction, we used our best-fit uniform disk and Gaussian model as the initial image. In both of these cases, we find a larger amount of flux in the central region of the image and a more compact size for the extended emission, compared to the two-component geometric models. This could suggest that the boundary between the star and the wind is more blurred than in our simpler models. However, this could also be the result of the software having difficulty reconstructing a sharper boundary between the "edge" of the star and the fainter, more diffuse emission. The faint, extended tails in the north–south and east–west directions line up roughly with gaps in the (u, v) coverage (compare the images with combined coverage for 2010–2011 in Figure 3) and are most likely artifacts produced in the reconstruction process. The generation of such artifacts could also be influenced by small, baseline-dependent calibration errors, such as the visibilities near $B/\lambda \sim (50\text{–}70) \times 10^6$ in Figure 4, which are systematically below the model fit.

The MACIM software allows for simultaneously fitting for a uniform disk while reconstructing the extended emission. Including a uniform disk with a diameter of 0.411 mas that contributes 55% of the flux, MACIM produced the images in the lower panels of Figure 7. For both reconstructions, we used the Gaussian component of our two-component model as the initial image for the extended emission. MACIM offers the flexibility of using different regularizers that reduce the weighting for non-physical images by balancing the tasks of lowering the χ^2 statistic while optimizing the regularization statistic. The image on the lower left of Figure 7 used the MACIM option

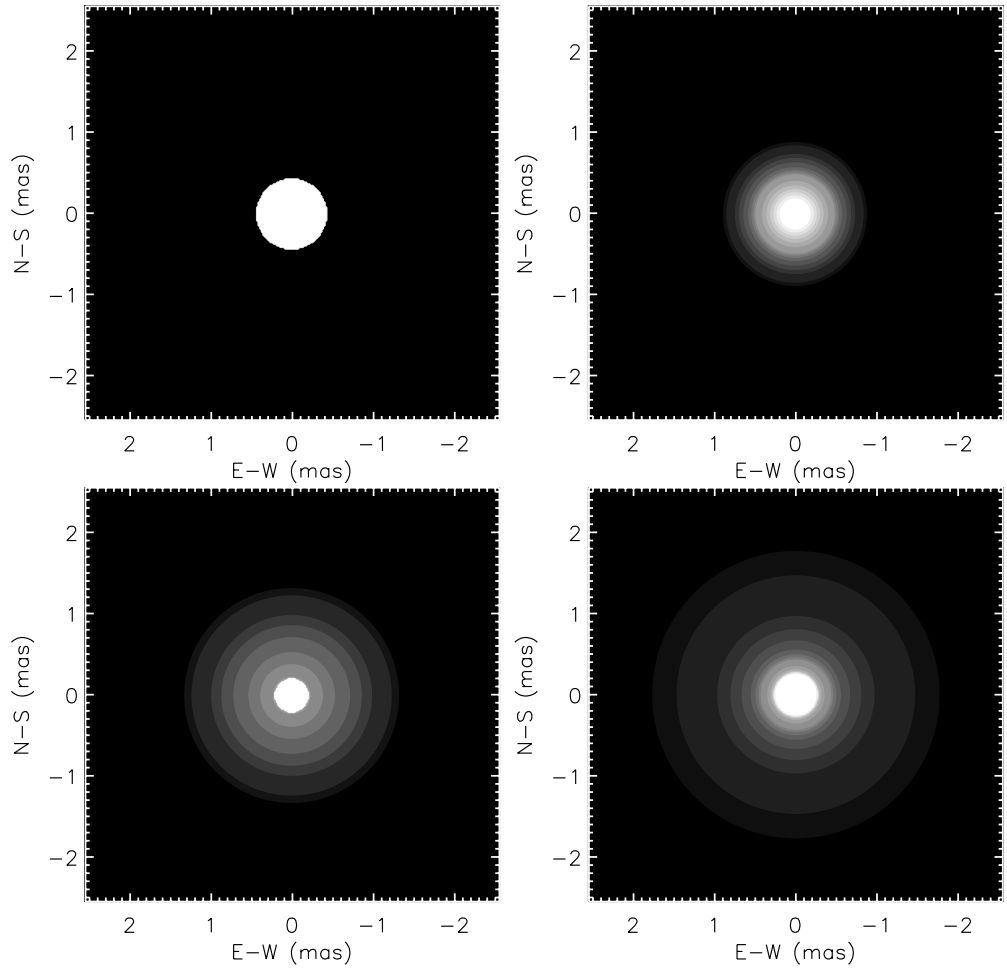

Figure 6. Model flux distributions of P Cyg fit to the interferometric visibilities in the combined data from 2010 to 2011: a uniform disk (upper left), a circularly symmetric Gaussian (upper right), and a two-component model (bottom left). In the bottom right we show the flux distribution of the CMFGEN model scaled to optimize the fit to the interferometric visibilities (the visibility curve shown in Figure 4). Contour intervals are drawn at 0.01%, 0.05%, 0.1%, 0.5%, 1%, 2%, 4%, 6%, 8%, 10%, 20%, 30%, 40%, and 50% of the peak flux in each panel (contours extend up to 60% and 70% of the peak flux for the circular Gaussian and 60%, 70%, and 80% of the peak flux for the CMFGEN model).

of a "compressed sensing regularizer," which minimizes spatial gradients in the image (e.g., Donoho 2006; Candes & Tao 2006). For the image on the lower right, we used our Gaussian model as a prior to define the probability for where the emission might be located, in order to keep the emission more centrally located. In both cases, the sharp edge between the star and the wind is retained because we included a fixed uniform disk in the reconstruction process. These images show that the *H*-band emission from the wind of P Cygni is largely spherical and consistent with the overall size and shape that we derived from our geometric model.

In Figure 5, we overplotted the closure phases computed from the image in the lower-left panel of Figure 7. All of the image reconstructions, for the combined data set as well as the individual epochs, provide reasonable fits to the small, non-zero closure phases, but unfortunately, we could not find a unique solution to describe the location and shape of a slight asymmetry in the wind. The nearly point-symmetric morphology of P Cygni (with closure phases close to 0°) makes it difficult to constrain the detailed structure of the wind. Additionally, diffuse emission from an extended, Gaussian envelope is a difficult case for interferometric imaging, because the image reconstruction techniques can generate artifacts associated with gaps in the frequency coverage.

Vakili et al. (1997) examined P Cygni interferometrically using the GI2T in the Hα and He I λ6678 lines. They deduced that there was a structure in the wind located at a projected radial separation of $R \approx 4R_\star$ (0.8 mas) away from the star. The angular resolution (FWHM) of the CHARA Array with the MIRC beam combiner is ≈0.5 mas, so we should detect such a structure if it is relatively bright compared to the star and wind. The closure phase (in radians) is $\approx F_{\rm asymmetric}/F_{\rm symmetric}$ (Monnier 2007), and our results (see Figure 5) show that the largest closure phase we measure is ∼2°, or 0.035 rad. If we assume the entire closure phase quantity is due to a single asymmetry in the wind (such as a blob or clump), then any such blob would contribute less than about 4% of the symmetric stellar and wind flux. According to our models of the wind halo (Figure 8), the wind flux at $R = 0.8$ mas is quite faint in the *H* band (only about 1% of the maximum light). Consequently, observations like ours would only detect rather extreme and isolated wind density enhancements (i.e., a distribution of clumps surrounding the star would yield a smaller net closure phase because the flux distribution would appear more symmetrical).

3.4. Limits on the Presence of a Binary Companion

Kashi (2010) argued that seventeenth century eruptions of P Cygni might have resulted from an interaction with a B-type,

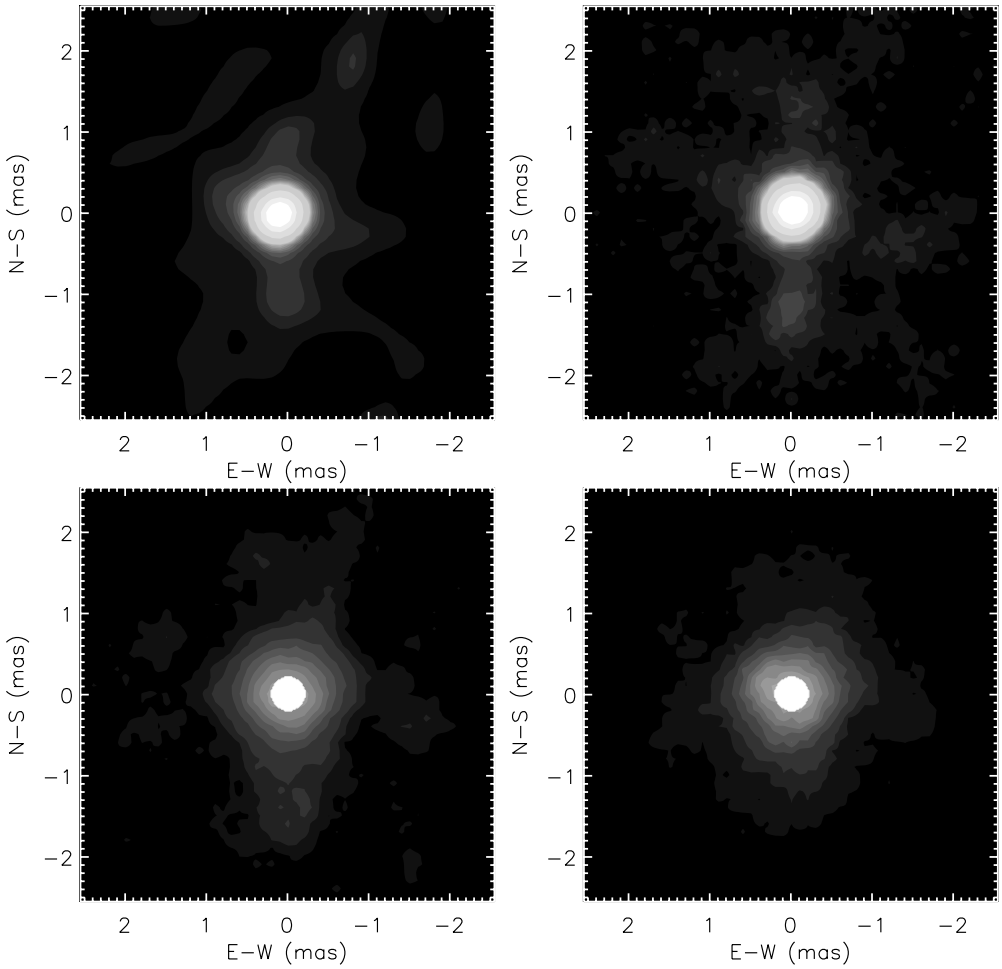

Figure 7. Image reconstructions of P Cygni based on our MIRC data from 2010 to 2011 (240 visibility measurements and 232 closure phase measurements). Top left: image reconstruction from BSMEM using a 2.0 mas Gaussian as the initial image and prior ($\chi^2_{V^2} = 331.4$ for the visibilities and $\chi^2_{\rm CP} = 70.4$ for the closure phases, where the χ^2 is calculated as the number of observations minus the degree of the fit). Top right: image reconstruction from MACIM using our two-component geometric model as the initial image ($\chi^2_{V^2} = 267.1$, $\chi^2_{\rm CP} = 82.1$). Bottom left: MACIM image reconstruction of the extended emission while fitting for a uniform disk of 0.41 mas that contributes 55% of the light ($\chi^2_{V^2} = 218.7$, $\chi^2_{\rm CP} = 86.1$). This reconstruction used the Gaussian component of our two-component model as the initial image and used a regularizer to minimize spatial gradients in the reconstructed image. Bottom right: MACIM image reconstruction of the extended emission made assuming a stellar flux component with a UD of 0.41 mas that contributes 55% of the light ($\chi^2_{V^2} = 194.9$, $\chi^2_{\rm CP} = 103.1$). This reconstruction used the Gaussian component from our two-component model as the initial image and as a prior to define the probability for how the flux moves during the reconstruction process. Contour intervals are drawn at 0.05%, 0.1%, 0.5%, 1%, 2%, 3%, 4%, 5%, 6%, 7%, 8%, 9%, 10%, 20%, 40%, and 60% of the peak flux in each panel. In all cases, the χ^2 calculated from the closure phases is smaller than the number of measurements. However, we suspect that this is the result of the closure phases being so close to 0 and that small movements in the flux during the reconstruction process can reproduce the signal in many different ways, allowing the software to find a very precise, but not necessarily reliable, solution.

main-sequence star in a 7 yr, highly elliptical orbit. However, the historical light curve reported by de Groot (1988), which was used as a basis in these models, has been re-evaluated and has a more "typical" appearance of an LBV eruption (Smith et al. 2011) when viewed with a sparsely sampled light curve. While no periodic radial velocity variation was found in the recent high-resolution spectroscopic analysis over a 15 yr period by Richardson et al. (2011), the possibility of a binary is not eliminated given the high incidence of massive stars in binary systems (Mason et al. 2009). A companion in a 7 yr orbit would probably have an angular semimajor axis of approximately 6 mas for the probable distance and mass of P Cygni, and a binary with such a separation might be detectable in our interferometric observations.

To examine that possibility, the high-precision closure phases and visibilities measured with the MIRC beam combiner at the CHARA Array were evaluated to place limits on the presence of a binary companion to P Cygni. A binary star will produce a periodic signature in the visibilities and the closure phases, where the frequency of the variation depends on the separation of the components and the amplitude depends on their flux ratio (Boden 1999; Monnier 2007). We focused our efforts on the data set from 2011 September 3, to avoid the motion of the hypothetical companion between 2010 and 2011. Additionally, the 2011 data offer better (u, v) coverage and more closure phase triangles for computing the detection limits.

We investigated two possible scenarios. In both cases, we fixed the diameter of the primary stellar component to be 0.41 mas (75 $R_\odot$) and assumed that the secondary is a point source. In the first scenario, we explored whether the small, non-zero closure phases could be accounted for by a binary companion alone. We used our two-component uniform disk and symmetric Gaussian model of the wind emission optimized for the 2011 epoch ($\theta_{\rm FWHM} = 0.898$ mas). We then fit for a binary system by searching through a grid of separations in R.A. and decl. over a range of ± 14 mas and solving for the

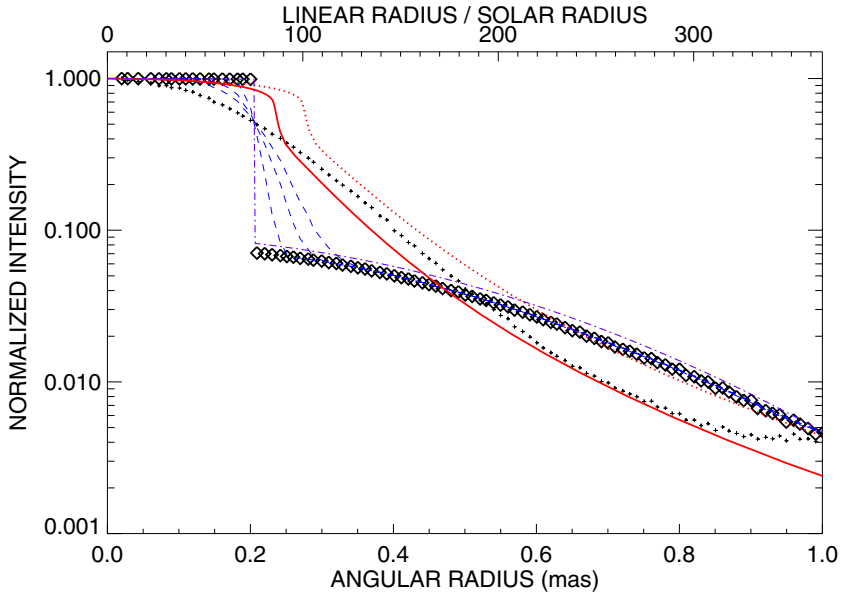

Figure 8. Theoretical light distribution of the star and wind in the *H* band from CMFGEN models (red solid curve) directly from the CMFGEN model, as well as a rescaled version from a fit to the visibility curve (red dotted curve). The average radial profile of the MACIM image reconstruction (lower-left panel of Figure 7) is shown by the diamond symbols, along with Gaussian-smoothed versions of the reconstruction over 10%, 20%, and 30% of the stellar radius (blue dashed lines). The purple dot-dashed curve represents the two-component model derived from the visibilities. Finally, the radial distribution of the flux from the image reconstruction with no regularizer and no uniform disk component (top right image of Figure 7) is plotted as plus signs.

(A color version of this figure is available in the online journal.)

secondary-to-primary flux ratio of the binary at each step. We also allowed the flux contributions from the primary star and its wind to vary in order to accommodate the additional flux from the hypothetical secondary. We ran through two iterations of the grid search: on the first pass we used a step size of 0.2 mas in separation and allowed the R.A. and decl. separations to vary to their best-fit values; on the second pass we used a fixed step size of 0.01 mas to finely map the χ^2 surface near the location of the absolute minimum. Using this approach, we found a best-fit binary solution where the agreement with the visibilities is similar to the symmetric two-component model and the χ^2 calculated from the closure phases is reduced from 198.4 for the symmetric model, where we do not fit for the closure phases, to $\chi^2_{\rm CP} = 99.5$ when including a binary companion (based on 160 closure phase measurements). However, the image reconstructions for this epoch give a χ^2 calculated from the closure phases of only ∼54.8. Therefore, while a binary companion could account for some of the non-zero closure phase signal, the image reconstructions that map the fine-scale structure in the wind do a better job of fitting the data. Based on the analysis of the binary fits with a two-dimensional Gaussian wind, we estimate that any possible binary companion must be more than 4.9 mag fainter than the central star in P Cygni or 5.6 mag fainter than the star+wind combined.

In the second scenario, we selected an MACIM image reconstruction of the wind assuming a uniform disk central star for the data from 2011 September 3 and investigated whether adding a binary component would improve the fit. We added in a binary model to the image of the wind and searched through a grid of separations in R.A. and decl. over a range of ±14 mas and solved for the secondary-to-primary flux ratio of the binary at each step while allowing the flux contribution from the wind to vary. We found a best-fit binary solution where the total χ^2 calculated from the visibilities and closure phases is reduced from 154.3 ($\chi^2_{V^2} = 99.5$, $\chi^2_{\rm CP} = 54.8$) for the image+UD to $\chi^2 = 145.5$ ($\chi^2_{V^2} = 93.6$, $\chi^2_{\rm CP} = 51.9$) when including a binary companion (based on 120 visibilities and 160 closure phase measurements). Performing an *F*-test on the ratio of the reduced χ^2_ν values (0.527/0.553 = 0.95), we find that this ratio can be exceeded by about 35% of random observations, suggesting that the improvement in the fit by adding the binary parameters is not significant. Based on the analysis of the binary fits using the reconstructed image of the wind, we find a tighter restriction on the presence of a binary companion in that it must be more than 5.3 mag fainter than the central star or 6.0 mag fainter than the star+wind combined in the *H* band.

We can estimate the absolute magnitude of the LBV star in P Cygni and then determine limits on the kinds of faint companions that remain undetected. Based upon the *H*-band flux measurements given in Table 2 and the calibration of Cohen et al. (2003), we estimate that the apparent *H*-band magnitude was 3.28 ± 0.09 during 2010–2011. Then, given the distance and reddening from Najarro et al. (1997), the absolute *H*-band magnitude at that time was −8.14 ± 0.15 for the LBV and its wind, or −7.49 ± 0.15 for the LBV alone (based upon the flux fraction from the results for the two-component model in Table 5). The $\triangle H = 5.3$ mag limit from above then suggests that we would have probably detected any main-sequence star brighter than $H = -2.2$ mag. This magnitude corresponds approximately to that of a B1 V star (Cox 2000). Thus, our results appear to rule out main-sequence companions of types O to B0V, but not later. In all cases, a secondary star very close (within a few R_*) to the primary would blend with the primary and would be undetectable. Future studies with more CHARA/MIRC data utilizing all six telescopes will produce stronger constraints on the absence of a companion. The number of known LBVs with a stellar companion is small (Martayan et al. 2012; Vink 2012). While this analysis does not disprove the Kashi (2010) conjecture, the improved light curve of the eruption shown by Smith et al. (2011), the lack of periodic

radial velocity variation found by Richardson et al. (2011), and this analysis point toward a single-star nature for P Cygni.

4. DISCUSSION AND CONCLUSIONS

Our CHARA Array observations provide the first high angular resolution look at the LBV P Cygni in the *H*-band continuum. We find that the angular size of the wind is much larger than the 0.41 mas diameter predicted for the photosphere from spectral models and the distance of the star (Najarro et al. 1997; Najarro 2001). A spatial flux model consisting of a uniform disk photosphere and a circular Gaussian halo provides an excellent match to the interferometric observations. The halo probably corresponds to flux emitted in the base of the stellar wind of P Cygni. The FWHM of the halo light is approximately 1 mas, which is smaller than the 5.5 mas size found for the Hα emission (formed over a larger wind volume because of its higher optical depth; Vakili et al. 1997).

The two-component model also provides an estimate of the relative flux contributions of the star (uniform disk) and wind (circularly symmetric Gaussian), and the flux ratio of 1.36:1 (all epochs) from interferometry is consistent with that derived from spectrophotometry. The interferometry obtained in 2010 yields a ratio of $F_{\rm star}/F_{\rm wind} = 1.64 \pm 0.09$. This implies a predicted magnitude difference of $\triangle H = 2.5 \log[(F_{\rm wind} + F_{\rm star})/F_{\rm star}] = 0.52 \pm 0.05$ mag. Our spectrophotometry obtained within a month of the 2010 interferometric data shows an excess of $\triangle H = 0.55 \pm 0.01$ mag (Table 2), in excellent agreement with the interferometric results. Thus, the SED models used to determine the IR flux excess and the geometric models used in the interferometric analysis agree within the uncertainties.

Our interferometric results obtained with the MIRC instrument and the CHARA Array include precise closure phases (Figure 5). These measurements reveal the possibility of a small amount of asymmetry present in the wind and may help probe the geometry of the stellar wind outflow. From image reconstructions, we found there may be some wind asymmetry (as indicated by small non-zero closure phases), but the wind is spherical within observational limits. It may be possible in future studies, with more complete coverage of the (u, v) plane than we obtained (Figure 3), to determine the exact location of any bright asymmetries in the wind. The image reconstruction process could also be aided by the development of a regularizer that would keep the image smooth in azimuth in order to avoid the problem of diffuse, extended emission from mapping onto gaps in the (u, v) coverage.

Models of LBV atmospheres and winds can accurately reproduce the emergent spectra (Najarro et al. 1997; Hillier & Miller 1998). We utilized the CMFGEN model of P Cygni with the parameters of Najarro (2001) to compare the theoretical visibility curve with the observed visibility curve (Figure 4). We computed the visibility curve for the derived wind radial light distribution in the *H*-band continuum for the adopted mass-loss rate $\dot{M} = 3.2 \times 10^{-5}\, M_{\odot}\, {\rm yr}^{-1}$, a stellar radius of $76\, R_{\odot}$, and a distance of 1.7 kpc. The CMFGEN model predicts a radial profile with a half-width at half-maximum of $R/R_{\odot} = 88$ (Figure 8). However, the visibilities associated with the model made a poor match with the observed values, so we rescaled the angular size until it best matched the visibilities (Figure 4). This resulted in the CMFGEN model being scaled 17% larger than expected. We overplot the visibilities of the scaled CMFGEN model as the dotted red line in Figure 4, and show the scaled model for comparison in Figure 6. The resulting agreement has a reduced χ^2_{ν} of 1.5, only marginally worse than that of our two-component model ($\chi^2_{\nu} = 1.1$). The major deviation in the scaled curve is at the largest baselines, where we sample the smallest angular scales. We also used this scaled CMFGEN model as an initial image for image reconstruction, and we found that the resulting image was nearly identical to that which used our two-component model as the initial image.

We compare the calculated radial light distribution from the CMFGEN model to our radial distribution from the image reconstructions in Figure 8. The radial profile from our reconstructed images includes a sharp edge from the star. In reality, the sharp edge would be smoother due to effects of electron scattering and free–free emission. Therefore, in order to build a more realistic profile, we performed a Gaussian smoothing to the images. The smoothed profiles appear similar to the predicted profile from the CMFGEN models, but the scales of the inner light distribution differ. However, we caution that the angular resolution of our interferometry is insufficient to differentiate between the models at scales $\leqslant$0.5 mas. The general agreement at large scales shows that the CMFGEN model prediction about the spatial distribution of the wind flux is consistent with our observations.

The model radial intensity distribution had to be rescaled to fit the visibilities, which resulted in a size about 17% larger than the predicted size. There are several plausible explanations for this difference. First, P Cygni could be closer to us than the assumed distance of 1.7 kpc, so that its angular size appears larger. Second, there are a large number of hydrogen emission lines in the *H* band (see Figure 1) that form in the wind at larger radii than the continuum flux. The emission lines are blended with the continuum flux in our low spectral resolution observations with MIRC ($R \sim 42$), but their net contribution may lead to an overestimate of the size of the spatial intensity distribution compared to what would be observed for the continuum alone. Finally, it is possible that some adjustments to the wind model could account for the difference in the angular size of the wind flux (if the above reasons are insufficient). The mass-loss rate of P Cygni is known to vary (e.g., Richardson et al. 2011), and the observed Hα strength was high during the second epoch of CHARA observations (Figure 2). This might indicate that the actual mass-loss rate was larger than the assumed model value. In addition, small changes related to the assumed velocity law and/or wind clumping factor could also lead to differences in the angular size prediction comparable to the observed difference.

Our results represent the first images of the circumstellar environs close to the prototypical LBV, P Cygni. The wind appears to be spherically symmetric. The results of the interferometric analysis and the spectroscopic analysis are mutually consistent, so long-term temporal variations in wind emission should also be detected in spatial observations through interferometry. P Cygni should remain a prime target for monitoring with optical and NIR spectroscopy, photometry, and improved interferometry.

We acknowledge with thanks the variable star observations from the AAVSO International Database contributed by observers worldwide and used in this research. Support for Ritter Astrophysical Research Center during the time of the observations was provided by the National Science Foundation Program for Research and Education with Small Telescopes (NSF-PREST) under grant AST-0440784 (N.D.M.). This work was also supported by the National Science Foundation under grants AST-0606861 and AST-1009080 (D.R.G.). N.D.R. gratefully acknowledges his current CRAQ postdoctoral fellowship.

We are grateful for the insightful comments of A. F. J. Moffat that improved portions of the paper, discussions with Paco Najarro and Luc Dessart about spectroscopic modeling of P Cygni, and support of the MIRC 6 telescope beam combiner by Ettore Pedretti. Institutional support has been provided by the GSU College of Arts and Sciences and by the Research Program Enhancement fund of the Board of Regents of the University System of Georgia, administered through the GSU Office of the Vice President for Research. Operational funding for the CHARA Array is provided by the GSU College of Arts and Sciences, by the National Science Foundation through grants AST-0606958 and AST-0908253, by the W. M. Keck Foundation, and by the NASA Exoplanet Science Institute. We thank the Mount Wilson Institute for providing infrastructure support at Mount Wilson Observatory. The CHARA Array, operated by Georgia State University, was built with funding provided by the National Science Foundation, Georgia State University, the W. M. Keck Foundation, and the David and Lucile Packard Foundation. This research was conducted in part using the Mimir instrument, jointly developed at Boston University and Lowell Observatory and supported by NASA, NSF, and the W. M. Keck Foundation. J.D.M. acknowledges University of Michigan and NSF AST-0707927 for support of MIRC construction and observations. D.P.C. acknowledges support under NSF AST-0907790 to Boston University. We gratefully acknowledge all of this support. This research has made use of the SIMBAD database operated at CDS, Strasbourg, France.

Facilities: Ritter Observatory, AAVSO, Perkins, IRTF, CHARA, HLCO

REFERENCES

Balan, A., Tycner, C., Zavala, R. T., et al. 2010, AJ, 139, 2269
Barnes, T. G., Evans, D. S., & Moffett, T. J. 1978, MNRAS, 183, 285
Baron, F., & Young, J. S. 2008, Proc. SPIE, 7013, 121
Boden, A. F. 1999, in Principles of Long Baseline Interferometry, ed. P. R. Lawson (Pasadena, CA: JPL), 9
Bonneau, D., Clausse, J.-M., Delfosse, X., et al. 2006, A&A, 456, 789
Candes, E. J., & Tao, T. 2006, ITIT, 52, 5406
Che, X., Monnier, J. D., & Webster, S. 2010, Proc. SPIE, 7734, 91
Che, X., Monnier, J. D., Zhao, M., et al. 2011, ApJ, 732, 68
Chesneau, O., Roche, M., Boccaletti, A., et al. 2000, A&AS, 144, 523
Clemens, D. P., Sarcia, D., Grabau, A., et al. 2007, PASP, 119, 1385
Cohen, M., Wheaton, Wm. A., & Megeath, S. T. 2003, AJ, 126, 1090
Cox, A. N. 2000, Allen's Astrophysical Quantities (4th ed.; New York: AIP)
Cushing, M. C., Vacca, W. D., & Rayner, J. T. 2004, PASP, 116, 362
de Groot, M. 1988, IrAJ, 18, 163
Donoho, D. L. 2006, ITIT, 52, 1289
Gies, D. R., Bagnuolo, W. G., Jr., Baines, E. K., et al. 2007, ApJ, 654, 527
Hillier, D. J., & Miller, D. L. 1998, ApJ, 519, 354
Humphreys, R. M., & Davidson, K. 1994, PASP, 106, 1025
Ireland, M. J., Monnier, J. D., & Thureau, N. 2006, Proc. SPIE, 6268, 58
Israelian, G., & de Groot, M. 1999, SSRv, 90, 493
Kashi, A. 2010, MNRAS, 405, 1924
Kervella, P., & Fouqué, P. 2008, A&A, 491, 855
Lamers, H. J. G. L. M., & Cassinelli, J. P. 1999, Introduction to Stellar Winds (Cambridge: Cambridge Univ. Press)
Markova, N., Morrison, N., Kolka, I., & Markov, H. 2001, A&A, 376, 898
Martayan, C., Lobel, A., Baade, D., et al. 2012, in ASP Conf. Ser. 464, Circumstellar Dynamics at High Resolution, ed. A. Carciofi & Th. Rivinius (San Francisco, CA: ASP), 293
Mason, B. D., Hartkopf, W. I., Gies, D. R., Henry, T. J., & Helsel, J. W. 2009, AJ, 137, 3358
Monnier, J. D. 2007, NewAR, 51, 604
Monnier, J. D., Berger, J.-P., Millan-Gabet, R., & ten Brummelaar, T. 2004, Proc. SPIE, 5491, 1370
Monnier, J. D., Pedretti, E., Thureau, N., et al. 2006, Proc. SPIE, 6268, 55
Monnier, J. D., Zhao, M., Pedretti, E., et al. 2007, Sci, 317, 342
Morrison, N. D., Knauth, D. C., Mulliss, C. L., & Lee, W. 1997, PASP, 109, 676
Najarro, F. 2001, in ASP Conf. Ser. 233, P Cygni 2000: 400 Years of Progress, ed. M. de Groot & C. Sterken (San Francisco, CA: ASP), 131
Najarro, F., Hillier, D. J., & Stahl, O. 1997, A&A, 326, 1117
Pauls, T. A., Young, J. S., Cotton, W. D., & Monnier, J. D. 2005, PASP, 117, 1255
Percy, J. R., Evans, T. D. K., Henry, G. W., & Mattei, J. A. 2001, in ASP Conf. Ser. 233, P Cygni 2000: 400 Years of Progress, ed. M. de Groot & C. Sterken (San Francisco, CA: ASP), 31
Pollmann, E., & Bauer, T. 2012, JAVSO, 40, 894
Rayner, J. T., Toomey, D. W., Onaka, P. M., et al. 2003, PASP, 115, 362
Richardson, N. D., Morrison, N. D., Gies, D. R., et al. 2011, AJ, 141, 120
Schaefer, G. H., Gies, D. R., Monnier, J. D., et al. 2010, AJ, 140, 1838
Skinner, C. J., Becker, R. H., White, R. L., et al. 1998, MNRAS, 296, 669
Skinner, C. J., Exter, K. M., Barlow, M. J., Davis, R. J., & Bode, M. F. 1997, MNRAS, 288, L7
Smith, N., Li, W., Silverman, J. M., Ganeshalingam, M., & Filippenko, A. V. 2011, MNRAS, 415, 773
ten Brummelaar, T. A., McAlister, H. A., Ridgway, S. T., et al. 2005, ApJ, 628, 453
Touhami, Y., Richardson, N. D., Gies, D. R., et al. 2010, PASP, 122, 379
Vacca, W. D., Cushing, M. C., & Rayner, J. T. 2003, PASP, 115, 389
Vakili, F., Mourard, D., Bonneau, D., Morand, F., & Stee, P. 1997, A&A, 323, 183
van Genderen, A. M. 2001, A&A, 366, 508
Vink, J. S. 2012, in Eta Carinae and the Supernova Imposters, ed. K. Davidson & R. M. Humphreys (Astrophysics and Space Science Library, Vol. 384; Dordrecht: Springer), 221
Weigelt, G., Kraus, S., Driebe, T., et al. 2007, A&A, 464, 87
Zorec, J., Cidale, L., Arias, M. L., et al. 2009, A&A, 501, 297